

Search for gravitational waves from 12 young supernova remnants with a hidden Markov model in Advanced LIGO's second observing run

Margaret Millhouse^{✉,*}, Lucy Strang, and Andrew Melatos

OzGrav, School of Physics, University of Melbourne, Parkville, Victoria 3010, Australia

 (Received 17 March 2020; accepted 25 September 2020; published 21 October 2020)

Persistent gravitational waves from rapidly rotating neutron stars, such as those found in some young supernova remnants, may fall in the sensitivity band of the Advanced Laser Interferometer Gravitational-wave Observatory (aLIGO). Searches for these signals are computationally challenging, as the frequency and frequency derivative are unknown and evolve rapidly due to the youth of the source. A hidden Markov model (HMM), combined with a maximum-likelihood matched filter, tracks rapid frequency evolution semicoherently in a computationally efficient manner. We present the results of an HMM search targeting 12 young supernova remnants in data from Advanced LIGO's second observing run. Six targets produce candidates that are above the search threshold and survive predefined data quality vetoes. However, follow-up analyses of these candidates show that they are all consistent with instrumental noise artifacts.

DOI: [10.1103/PhysRevD.102.083025](https://doi.org/10.1103/PhysRevD.102.083025)

I. INTRODUCTION

Young supernova remnants (SNRs) hosting rotating neutron stars are promising candidates for the detection of continuous gravitational waves (GWs) by the Advanced Laser Interferometric Gravitational-wave Observatory (aLIGO) [1–3]. Detection of transient GW events from mergers of compact binaries has now become routine [4]. Persistent, periodic GW signals have not yet been detected, but they are an attractive target, because the GW strain is proportional to the stellar ellipticity, which is determined partly by the nuclear equation of state [1]. Motivated by the opportunity to do fundamental nuclear physics experiments, several groups have conducted continuous wave searches covering the whole sky [5–7] and various specific targets, e.g., known pulsars [8,9], the Galactic center [10,11], and young SNRs [12–15], which are the subject of this paper.

Young neutron stars are especially likely to be non-axisymmetric, as any ellipticity produced during the violent birth of the star has had less time to relax by Ohmic, viscous, or tectonic processes [16–18]. Mass quadrupole emission (e.g., thermoelastic [19,20] or magnetic [21–23] mountains) is expected to occur at the neutron star's rotational frequency, f_* , or $2f_*$. Current quadrupole emission, e.g., from a pinned superfluid [24,25] or r modes [26], is expected to occur at f_* or approximately $4/3f_*$, respectively.

Traditional searches are hampered by the computational cost of trialing a huge number of matched filters, when the spin frequency and its evolution are rapid and unknown.

The computing cost for these searches scales as $f_{\max}^{2.2} a^{-1.1} T_{\text{obs}}^4$ [27], where a is the age of the neutron star, f_{\max} is the highest frequency in the search band, and T_{obs} is the total length of the observation. This makes searches on long stretches of data (e.g., $T_{\text{obs}} \gtrsim 1$ yr) with unknown frequency evolution for young neutron stars computationally infeasible. Neutron stars are also subject to timing noise [28], which causes the signal to wander stochastically.

In this paper, we present the results of a hidden Markov model (HMM) search for continuous waves first introduced by Suvorova *et al.* in 2016 [29], using open data from Advanced LIGO's second observing run [30,31]. The HMM is both robust against spin wandering and computationally cheap.

The paper is organized as follows. In Sec. II A we give an overview of the methods used in previous searches for GWs from SNRs. In Sec. II C we introduce the HMM and describe how the HMM formalism is used in the search for continuous GWs. Section III explains the methodology for selecting the search parameters for each SNR. In Sec. IV A we go over the selection of SNR targets, and in Sec. IV B we introduce the methods for selecting a threshold for detection. Section V presents the results of our search, including the requirements for vetoing a potential candidate. We conclude in Sec. VI.

II. METHODOLOGICAL OVERVIEW

A. Previous SNR searches

Three searches for continuous GWs from SNRs were performed in data from Initial LIGO [14,27,32,33]. More recently, three searches have been performed for

*meg.millhouse@unimelb.edu.au

GW emission from young SNRs in Advanced LIGO's first and second observing runs (O1 and O2, respectively) [12,13,15]. No detections were reported, and upper limits were set on the maximum GW strain emitted by each target. Because O1 and O2 are more sensitive than Initial LIGO, Refs. [12,15] improve significantly upon the upper limits set in Ref. [27].

B. Matched filter

Some of the previous searches [12,15,27,32] used a coherent matched-filter test that was based on the maximum-likelihood \mathcal{F} -statistic [34]. The \mathcal{F} -statistic also plays an important role in the HMM search in this paper.

In the \mathcal{F} -statistic formulation, the detector data $d(t)$ are modeled as a GW signal $h(t)$ plus stationary noise $n(t)$, or explicitly

$$d(t) = h(t) + n(t). \quad (1)$$

The log-likelihoods of the signal (\mathcal{H}_1) and null (\mathcal{H}_0) hypotheses, respectively, are given by

$$p(d|\mathcal{H}_1) = -\frac{1}{2} \langle d - h | d - h \rangle \quad (2)$$

$$p(d|\mathcal{H}_0) = -\frac{1}{2} \langle d | d \rangle, \quad (3)$$

where $\langle x|y \rangle$ is the noise-weighted inner product, defined as

$$\langle x|y \rangle = 4\text{Re} \int_0^\infty \frac{\tilde{a}(f)\tilde{b}^*(f)}{S_n(f)} df. \quad (4)$$

Here $S_n(f)$ is the one-sided noise power spectral density, and a tilde denotes the Fourier transform. The log-likelihood ratio of the signal $h(t)$ given the data $d(t)$ can then be written as

$$\log \Lambda = \langle d|h \rangle - \frac{1}{2} \langle h|h \rangle. \quad (5)$$

For a persistent GW signal of constant amplitude, $h(t)$ can be written as

$$h(t) = \sum_{\mu=1}^4 A^\mu h_\mu, \quad (6)$$

where A^μ are the amplitudes associated with h_μ . The h_μ are linearly independent and are given by

$$h_1 = a(t) \cos \Phi(t), \quad (7)$$

$$h_2 = b(t) \cos \Phi(t), \quad (8)$$

$$h_3 = a(t) \sin \Phi(t), \quad (9)$$

$$h_2 = b(t) \sin \Phi(t), \quad (10)$$

with $\Phi(t)$ giving the phase of the GW at the detector, accounting for the Doppler modulation of the signal due to the movement of Earth. The functions $a(t)$ and $b(t)$ are the antenna response functions of the detector and are written out explicitly in [34]. The log-likelihood ratio in Eq. (5) can then be expressed as

$$\log \Lambda = A^\mu d_\mu - \frac{1}{2} A^\mu A^\nu \mathcal{M}_{\mu\nu} \quad (11)$$

with $d_\mu \equiv \langle d|h_\mu \rangle$ and $\mathcal{M}_{\mu\nu} \equiv \langle h_\mu|h_\nu \rangle$.

The \mathcal{F} -statistic is a maximum-likelihood estimator, obtained by maximizing Eq. (11) with respect to A^μ , and is given by

$$\mathcal{F} = \frac{1}{2} d_\mu \mathcal{M}^{\mu\nu} d_\nu. \quad (12)$$

The random variable $2\mathcal{F}$ is drawn from a noncentral chi-squared distribution with four degrees of freedom:

$$\chi^2(2\mathcal{F}|4, \rho_0^2). \quad (13)$$

The noncentrality parameter ρ_0 is the optimal matched-filter signal-to-noise ratio.

To compute the \mathcal{F} -statistic, we use the ComputeFStatistic_v2 function that is part of the LIGO analysis library [35]. The details of this implementation can be found in Ref. [36]. This implementation combines data from both detectors. The noise spectral density $S_n(f)$ in Eq. (4) is estimated from the median of nearby frequency bins.

The \mathcal{F} -statistic template models the continuous GW signal as a sinusoid with slow frequency evolution given by

$$f(t_{\text{SSB}}) = f_* + \dot{f}_*(t_{\text{SSB}} - t_0) + \frac{1}{2} \ddot{f}_*(t_{\text{SSB}} - t_0)^2, \quad (14)$$

where t_0 is the time at the start of the observing period and t_{SSB} is the time at the Solar System barycenter. Equation (14) does not account for stochastic spin wandering on timescales of days to weeks, known as timing noise [37–39], which represents a major challenge for traditional \mathcal{F} -statistic searches. Additionally, the young neutron stars in this search may secularly spin down so rapidly that the template bank includes a wide range of f_* , \dot{f}_* , \ddot{f}_* even in the absence of spin wandering, leading to an unmanageable number of templates. Consequently, previous young SNR searches only use some of the available data. For example, O1 spanned 130 days, but the searched data in Ref. [12] only ranged from 3 to 44 days in the 15 targets [12]. The more recent \mathcal{F} -statistic search in O2 data spanned 12 to 55 days depending on the target and searched a frequency band of 15–150 Hz [15].

An alternative to a fully coherent matched-filter search is to break the data into smaller segments and perform a semicoherent analysis. A number of semicoherent analyses have been used in LIGO and Virgo searches for continuous GWs [40–42]. In this paper we perform a semicoherent search that uses an HMM to track the GW frequency. The HMM employs recursion to prune efficiently the exponentially large bank of templates required to capture rapid secular spin down or stochastic spin wandering.

C. HMM

An HMM relates a finite set of unobservable (“hidden”) discrete state variables to a finite set of observables. In this search, the hidden variable is the true GW frequency f_* , and the observable variable is the \mathcal{F} -statistic described in the previous section. We divide the full stretch of data of length T_{obs} into smaller segments of length T_{drift} , calculate the \mathcal{F} -statistic for each segment for a set of trial frequencies f_0 ,¹ and find the most likely evolution of the frequency, over the total observation time.

The set of hidden variables constitutes a Markov chain. A Markov chain describes a state $q(t)$ that wanders among a set of discrete states, $\{q_0, q_1, \dots, q_{N_Q}\}$, with state transitions happening at discrete time steps $\{t_0, t_1, \dots, t_{N_t}\}$. In this search, $q(t) = f_*(t)$, the true GW frequency. A Markov chain is memoryless, so the state at time t_i depends only on the state at the previous time step, t_{i-1} . The probability of a transition from one state to another is given by the transition probability

$$A_{q_j q_i} = P(q_j | q_i), \quad (15)$$

with $q(t_{n+1}) = q_j$ for some j and $q(t_n) = q_i$ for some i . In this search, we assume that from time step t_n to time step t_{n+1} , the frequency either stays in its current state ($q_j = q_i$), moves up one frequency bin ($q_j = q_{i+1}$), or moves down one frequency bin with equal probability ($q_j = q_{i-1}$), viz.

$$A_{q_i q_i} = A_{q_i q_{i+1}} = A_{q_i q_{i-1}} = \frac{1}{3}. \quad (16)$$

All other probabilities are zero.² Analyzing the data in segments eliminates the need to explicitly search over \dot{f}_0 and \ddot{f}_0 . The data segmentation also allows for a more flexible model of frequency evolution to account for stochastic spin wandering [44–47] and magnetic dipole

¹Here f_0 refers to the search frequency, i.e., the frequency in the argument of the \mathcal{F} -statistic, and f_* refers to the true frequency of the neutron star itself.

²Because young SNRs are expected to spin down rapidly [12,43], another choice would be $A_{q_i q_i} = A_{q_i q_{i-1}} = \frac{1}{2}$. To maximize flexibility and robustness, we choose to use Eq. (16). The extra computational burden is minimal, as confirmed in previous studies [29,43].

braking simultaneously, which is hard to achieve economically with a low-order Taylor expansion.

The observable $o(t)$ occupies one of the discrete states $\{o_0, o_1, \dots, o_{N_o}\}$. The observable state is related to the hidden state by an emission probability defined by

$$L_{o_i q_j} = P(o_i | q_j), \quad (17)$$

with $o(t_n) = o_i$ for some i and $q(t_n) = q_j$ for some j . The observable in this search is the \mathcal{F} -statistic. We calculate $\mathcal{F}(f_0)$ for each segment of length T_{drift} (the recipe for setting T_{drift} is described in Sec. III), at a frequency resolution of $\Delta f_0 = 1/(2T_{\text{drift}})$. The emission probability is given by [29]

$$L_{o(t) q_i} = P[o(t) | f_{0i} \leq f_0(t) \leq f_{0i} + \Delta f_0] \quad (18)$$

$$\propto \exp[\mathcal{F}(f_0)], \quad (19)$$

where f_{0i} is the value of f_0 in the i th frequency bin and the proportionality to the exponential follows from Eq. (13).

Over some observation period we can find the most likely hidden state sequence Q^* given the observable state sequence O by maximizing

$$P(Q|O) = L_{o(t_{N_t}) q(t_{N_t})} A_{q(t_{N_t}) q(t_{N_t-1})} \times \dots \times L_{o(t_1) q(t_1)} A_{q(t_1) q(t_0)} \Pi_{q(t_0)}, \quad (20)$$

with respect to Q . In Eq. (20), $\Pi_{q(t_0)}$ is the prior probability that the state started at q_i at $t = t_0$. As we do not know $f_0(t_0)$, the prior is uniform:

$$\Pi_{q(t_0)} = \frac{1}{N_Q}. \quad (21)$$

The maximization can be done with the Viterbi algorithm [48], which uses dynamic programming to sample the $N_Q^{N_t}$ sequences Q efficiently.

III. PARAMETERS

In this section we again outline the procedure for setting the parameters for an SNR search, namely the frequency range and T_{drift} .

A. Frequency range

The SNRs we are targeting in this paper do not contain electromagnetically observed pulsars, so $f_0(t)$ is unknown. We must therefore search over a broad range of frequencies. To set the frequency range, we demand that the indirect, age-based, spin-down upper limit on the GW strain lies above the strain sensitivity of the search. For a neutron star of age a at a distance D that is spinning down purely due to GW radiation, the characteristic strain h_0 satisfies $h_0 \leq h_0^{\text{max}}$ with [49]

$$h_0^{\max} = 1.26 \times 10^{-24} \left(\frac{3.3 \text{ kpc}}{D} \right) \sqrt{\frac{300 \text{ years}}{a}}. \quad (22)$$

On the other hand, assuming Gaussian noise, the 95% confidence upper limit on strain sensitivity for an incoherent search is analytically predicted to be (see Appendix E of [43])

$$h_0^{95\%} = \Theta S_n(f)^{1/2} (T_{\text{obs}} T_{\text{drift}})^{-1/4}, \quad (23)$$

where $\Theta \simeq 35$ is an empirical statistical factor [27,49] and $S_n(f)$ is the one-sided noise spectral density. In this paper we search over all f_0 satisfying $h_0^{\max} > h_0^{95\%}$ from Eqs. (22) and (23).

B. T_{drift}

The segment length T_{drift} is selected to minimize the mismatch in the \mathcal{F} -statistic. The mismatch is the fractional loss of signal power caused by the discretization of the parameters in the template set [50–52]. Previous HMM searches for low-mass x-ray binaries set $T_{\text{drift}} = 10$ days, the fiducial autocorrelation timescale for stochastic spin wandering in accreting systems [53–55]. An HMM has also been used to search for GWs from a long-lived remnant of a binary neutron star merger [56], which used a much shorter $T_{\text{drift}} = 1$ s, as the remnant is possibly spinning down very rapidly. In young SNRs hosting a nonaccreting neutron star, stochastic spin wandering with an autocorrelation timescale of days to weeks, known as timing noise in radio pulsar astronomy [44,57], must be weighed against rapid secular spin down.

As shown in detail in [43], for a neutron star with a spin-down rate of \dot{f}_* , in order to keep the \mathcal{F} -statistic mismatch below 0.2 when only searching over a constant f_0 (i.e., $\dot{f}_0 = 0$) in each coherent time segment, we require T_{drift} to satisfy

$$T_{\text{drift}} \leq (2|\dot{f}_*|)^{-1/2}. \quad (24)$$

Because the targets in this paper do not have visible pulsars, the spin-down rate \dot{f}_* is not known *a priori*. The range of \dot{f}_* to be used in this search can be found by considering the possible ranges of the braking index, $n = f_0 \ddot{f}_* / \dot{f}_*^2$. For a neutron star of characteristic age $a = f_* / [(n-1)\dot{f}_*]$, we have

$$-\frac{f_*}{(n_{\min} - 1)a} \leq \dot{f}_* \leq -\frac{f_*}{(n_{\max} - 1)a}, \quad (25)$$

where n_{\min} and n_{\max} are the minimum and maximum braking indices, respectively. Purely electromagnetic or gravitational braking implies $n = 3$ and $n = 5$, respectively. Current observations imply $2 \leq n \leq 7$ [46,58]. In this work

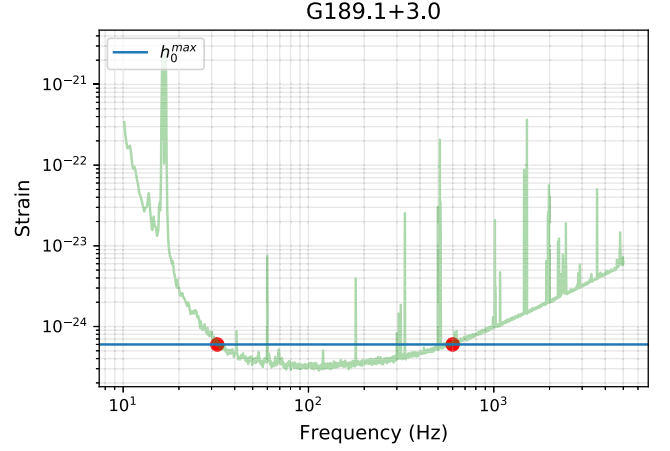


FIG. 1. Example of the predicted 95% upper limit $h_0^{95\%}$, from Eq. (23) (green curve), and the indirect upper limit h_0^{\max} , for the SNR G189.1 + 3.0. The red dots indicate f_{\min} and f_{\max} .

we assume $n = 2$ conservatively to capture the widest possible range of signals, yielding from Eq. (24):

$$T_{\text{drift}} = \left(\frac{a}{2f_*} \right)^{1/2}. \quad (26)$$

We note that Eq. (26) depends on f_* , which we do not know *a priori*. One option is to vary T_{drift} according to the search frequency f_0 , but this adds computational costs as well as additional trials factors. In this work we use a single T_{drift} per SNR target, which is the T_{drift} that corresponds to the highest frequency where $h_0^{\max} > h_0^{95\%}$.

C. Summary

The procedure for selecting T_{drift} and the frequency bounds (f_{\min} , f_{\max}) for each SNR target is as follows:

- (i) Insert Eq. (26) into Eq. (23) to predict $h_0^{95\%}$ for $10 \text{ Hz} < f_0 < 4000 \text{ Hz}$, which is approximately the frequency band where LIGO is sensitive.
- (ii) Calculate the indirect upper limit h_0^{\max} from Eq. (22).
- (iii) Find the highest frequency obeying $h_0^{\max} > h_0^{95\%}$; call it f_{\max} .
- (iv) Using Eq. (26), calculate T_{drift} for $f_0 = f_{\max}$.
- (v) Insert T_{drift} back into Eq. (23) and find the minimum frequency obeying $h_0^{\max} > h_0^{95\%}$; call it f_{\min} .

Figure 1 shows a predicted sensitivity curve and indirect h_0^{\max} for one example SNR. The green curve shows Eq. (23) for the calculated T_{drift} of two hours. The blue line is the indirect upper limit from Eq. (22), and the red points indicate f_{\min} and f_{\max} .

IV. IMPLEMENTATION

A. Target selection

In this work, we follow up on SNRs that have been targeted previously in LIGO data [12,27]. Recently, Ref. [12] searched O1 data for 15 young SNRs (as well

TABLE I. SNRs targeted in this search. For each target the table shows the astronomical parameters (RA, DEC, age, distance), search parameters (f_{\min} , f_{\max} , T_{drift} , and number of subbands), the indirect upper limit on the strain (h_0^{max}) and predicted maximum sensitivity at 95% confidence ($h_0^{95\%}$). For targets that are affected by the minimum T_{drift} of 1 h, we note in parentheses what the required T_{drift} would be without the condition $T_{\text{drift}} \geq 1$ h imposed. The final column gives the duty cycle, or the percentage of T_{drift} segments that had enough available data for at least the two SFTs required by the \mathcal{F} -statistic.

SNR	Age (kyr)	Distance (kpc)	f_{\min} (Hz)	f_{\max} (Hz)	T_{drift} (h)	h_0^{max} $\times 10^{-25}$	$h_0^{95\%}$ $\times 10^{-25}$	RA (J2000)	DEC (J2000)	Subbands	Duty cycle
G1.9 + 0.3 [61,62]	0.1	8.5	35	122	1.0 (0.5)	8.5	5.5	174846.9	-271016	61	69%
G18.9 - 1.1 [63,64]	4.4	2	34	505	3.3	5.4	3.5	182913.1	-125113	330	77%
G65.7 + 1.2 [65,66]	20	1.5	42	335	8.5	3.4	2.7	195217.0	292553	205	83%
G93.3 + 6.9 [67,68]	5.0	1.7	32	600	3.1	5.9	3.5	205214.0	551722	397	77%
G111.7 - 2.1 [69-71]	0.3	3.3	28	365	1.0 (0.6)	12	5.2	232327.9	584842	236	69%
G189.1 + 3.0 [72,73]	20	1.5	28	853	2.0	8.7	3.9	61705.3	222127	577	75%
G266.2 - 1.2 [74,75]	5.1	0.9	18	840	1.0 (0.4)	14	5.8	85201.4	-461753	575	69%
G291.0 - 0.1 [76,77]	1.2	3.5	36	471	1.7	5.9	4.0	111148.6	-603926	305	73%
G330.2 + 1.0 [78,79]	1.0	5	46	288	2.1	4.5	3.9	160103.1	-513354	169	74%
G347.3 - 0.5 [80-82]	1.6	0.9	23	1747	1.1	20	4.6	171328.3	-394953	1206	69%
G350.1 - 0.3 [83,84]	0.6	4.5	36	474	1.2	6.5	4.4	172054.5	-372652	307	70%
G354.4 + 0.0 [85]	0.5	8	28	122	1.0 (0.4)	14	6.0	173127.5	-333412	66	69%

as the neutron star Fomalhaut b). These SNRs were selected from the Green catalog [59]. Another recent search has followed up on a subset of these targets [15]. SNRs with central compact objects or pulsar wind nebulae are normally selected as they are likely hosts of neutron stars.

For each target, we select T_{drift} , f_{\min} , and f_{\max} as described in Sec. III B. The SNR targets and their respective search parameters are listed in Table I. The \mathcal{F} -statistic ingests data in the form of short Fourier transforms (SFTs) and requires at least two SFTs [60]. This leads to the condition that T_{drift} must be greater than twice the duration of the SFTs. The typical SFT duration used in previous continuous GW searches is 30 min, which requires $T_{\text{drift}} \geq 1$ h. As a result, the predicted sensitivity for some targets from Ref. [12] cannot beat the indirect upper limit, i.e., those that are young and spinning down rapidly. Additionally, f_{\max} for some targets is bounded by the minimum T_{drift} requirement rather than the sensitivity bounds in Sec. III B. While it is possible in principle to produce SFTs of shorter durations, it requires extra computational time and data storage, which exceed our computational resources.

The parameter space of many targets span decades in hertz, so we split the search into subbands to facilitate data handling as in previous work [53,54]. In this work we search over subbands of 2 Hz. This is wider than the subbands used previously (ranging from 0.606 to 1.0 Hz) because rapid spin down means the signal could transverse an entire subband during an interval of length T_{obs} if we use a width of 1 Hz or less. That is, there would be a high chance the signal would wander out of one subband, thereby decreasing the sensitivity of the search. The subbands overlap, so that when a Viterbi path does straddle two subbands it is completely contained in one of the two.

B. Detection statistic and threshold

Previous HMM searches used the Viterbi score [53,54] as the detection statistic. The Viterbi score is the number of standard deviations that the log-likelihood of a path deviates from the average of all the other paths in a given subband, where the log-likelihood is the sum of the values of the \mathcal{F} -statistic at each step along the Viterbi path. The Viterbi score ceases to be useful when the number of frequency bins, N_Q , becomes comparable to the number of time steps, N_T . To understand why, consider how the Viterbi algorithm finds the optimal path. By the principle of optimality [86], given an optimal path over N_T time steps that ends in frequency bin f_i , the optimal path that ends in frequency bin f_{i-1} (or f_{i+1}) is identical up to time step $N_T - 1$. More generally, two paths terminating j frequency bins apart have the same optimal subpath for time steps $1 < k < N_T - j$. For $N_Q \gg N_T$, we have $N_T - j < 0$ for most paths, so most of the suboptimal paths do not overlap. For $N_Q \gtrsim N_T$, however, many of the final paths converge onto the same suboptimal path. If this path is a loud signal, it increases the mean of the log-likelihoods of all paths, thereby artificially decreasing the Viterbi score. In short, in situations with $N_Q \gtrsim N_T$, the Viterbi score for a true signal counterintuitively gets worse for longer observation times. For this reason in this work we use the log-likelihood of the optimal path ending in each frequency bin as our detection statistic, unnormalized by the log-likelihoods of the neighboring paths. We denote the log-likelihood as \mathcal{L} .

The probability distribution function of \mathcal{L} of the optimal path is not known analytically; see Sec. III C of [29] for details. As verified empirically in Gaussian noise, the mean and standard deviation of \mathcal{L} depend only on N_T and scale in a well-behaved manner. Figure 2 shows the mean and standard deviation of the distribution of log-likelihoods in

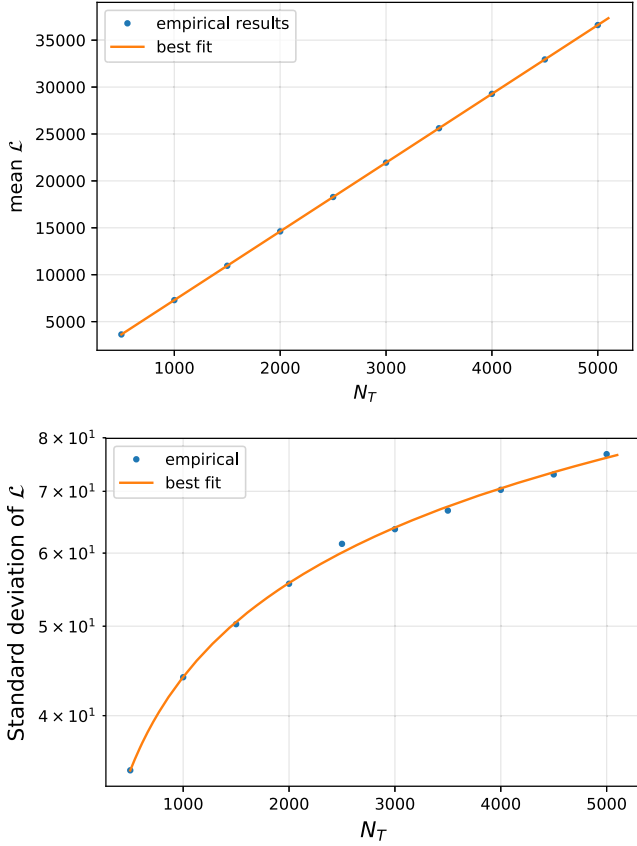


FIG. 2. The mean (top) and standard deviation (bottom) of \mathcal{L} of the optimal path in Gaussian noise versus the number of time steps N_T . The blue points are the empirical results. The orange curve is the best fit to those points.

100 realizations of Gaussian noise versus N_T for $500 \leq N_T \leq 5000$, relevant to the SNRs in this paper. We find that the mean of \mathcal{L} scales $\propto N_T$, and the standard deviation of \mathcal{L} scales $\propto N_T^{0.34}$.

We use the scalings in Fig. 2 to set the \mathcal{L} threshold \mathcal{L}_{th} . In this study we demand an overall false alarm probability of $\alpha_N = 0.01$ for each target across all of the relevant subbands, the standard used in previous HMM searches [53,54]. For each subband the desired false alarm probability α satisfies

$$\alpha_N = 1 - (1 - \alpha)^N, \quad (27)$$

where N is the number of subbands multiplied by N_Q .

The thresholds obtained from the above procedure are shown in Table II. The threshold range is $5761 \leq \mathcal{L}_{\text{th}} \leq 47783$. The threshold scales with the age of the SNR, so that targets of similar age have similar \mathcal{L}_{th} , though targets with many subbands incur more trials, thus increasing \mathcal{L}_{th} .

C. Data

In this work, we search data from LIGO's second observing run, spanning 270 calendar days from

November 2016 to August 2017. A third detector, Virgo, joined O2 for the last month. Due to the short duration of the Virgo run and its lower sensitivity, we analyze only data from the two LIGO detectors, Hanford and Livingston, in this paper. The strain data for O2 are publicly available from the Gravitational-wave Open Science Center [30,31,87].

During O2 the detectors had periods of downtime. There were two commissioning breaks during the run: an approximately two-week period between December and January and a break in May lasting 19 days for Livingston and 31 days for Hanford. In addition to these longer breaks, there were shorter periods of down time due to maintenance or environmental factors that brought the detectors out of lock. As described in the previous section, the SFT data products require at least 30 min of data, so stretches of data shorter than this are not used in the analysis. Furthermore, times in which the detector is known to not be properly operating in its nominal state are removed from the analysis [88,89]. Because the T_{drift} length periods used in this search are relatively short, there are sometimes T_{drift} length periods where there are no analyzable data. When this occurs, we fill in this period with a constant log-likelihood, as done in previous HMM searches [54]. Accounting for missing SFTs, the effective duty cycles for each SNR are listed in Table I.

V. RESULTS

All 12 of the targets in Table I return Viterbi scores above the threshold defined in Sec. IV B in some subbands. The number of outliers per target is summarized in the third column of Table II. \mathcal{L} of every outlier is plotted versus frequency in Fig. 3, colored by target.

Several of the outliers are likely to occur because the detector noise is not Gaussian, as assumed when setting the threshold in Sec. IV B. To distinguish real signals from

TABLE II. Threshold and the number of outliers above that threshold before and after applying the data quality vetoes.

SNR	\mathcal{L}_{th}	Outliers (preveto)	Outliers (postveto)
G1.9 + 0.3	47752	32	0
G18.9 - 1.1	14830	100	2
G65.7 + 1.2	5761	45	4
G93.3 + 6.9	15156	125	1
G111.7 - 2.1	47771	51	0
G189.1 + 3.0	23227	115	3
G266.2 - 1.2	47783	124	3
G291.0 - 0.1	27243	65	0
G330.2 + 1.0	23346	32	0
G347.3 - 0.5	45290	227	5
G350.1 - .03	47774	58	0
G354.4 + 0.0	47753	38	0

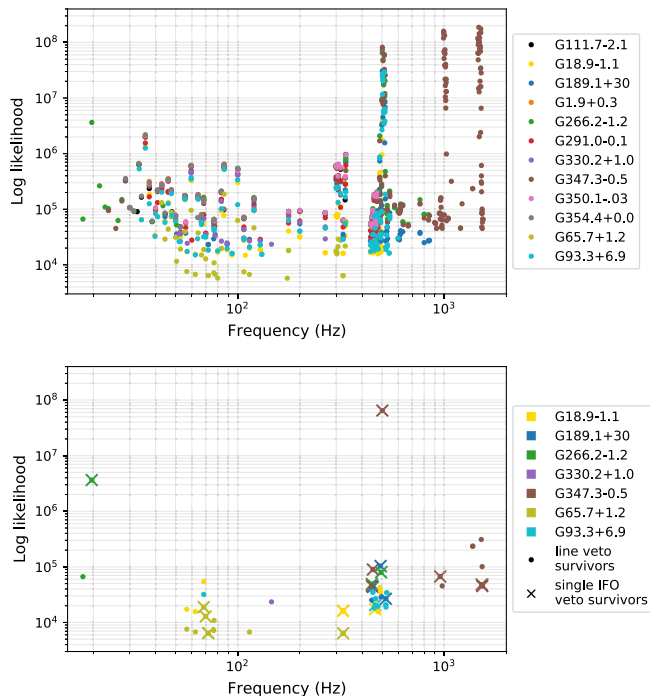


FIG. 3. Candidates whose log-likelihood exceeds the Gaussian threshold in Sec. IV B. \mathcal{L} is plotted against the terminating frequency of the associated Viterbi path, with points color coded by their corresponding target (see legend at right). Top: Candidates before vetoes. Bottom: Survivors after the known line veto (circles) and remaining candidates after the single interferometer (IFO) veto (crosses).

non-Gaussian noise, we pass the outliers through a set of vetoes used previously in published HMM searches [53,54].

A. Vetoes

Here we describe the vetoes in two categories. The motivating logic and implementation details for the vetoes are presented in Refs. [53,54].

- (i) *Instrumental noise lines*.—Narrow-band instrumental noise artifacts known as “lines” are present in LIGO data at both interferometer sites [90]. They are caused by suspensions vibrations and the electrical power grid among other things. We veto any candidate whose Viterbi path crosses the catalog of known instrumental lines [30].
- (ii) *Single-interferometer veto*.—An instrumental noise artifact that is present in one detector but not the other can artificially lift \mathcal{L} from both detectors combined, $\mathcal{L}_{2\text{ifo}}$, above the threshold \mathcal{L}_{th} . To identify these false alarms, we rerun the search for each outlying subband in each interferometer separately. If \mathcal{L} in either interferometer (but not both) exceeds $\mathcal{L}_{2\text{ifo}}$, we veto that candidate as an instrumental artifact. If neither of the single-interferometer log-likelihoods exceeds $\mathcal{L}_{2\text{ifo}}$, the candidate survives.

Previous HMM searches have included a veto category in which the search is rerun, dividing the data into two segments. A real signal should be significant in both segments and not turn on or off, although one can imagine exceptions, e.g., a transient r mode [26]. Previous searches however used the Viterbi score as a detection statistic [53,54], which (when meeting the requirements described in Sec. IV B) is independent of T_{obs} . Since our detection statistic depends on T_{obs} , we do not use this veto.

B. Survivors

The fourth column of Table III lists the veto survivors. There are 18 spread across six SNRs. We report the terminating frequency of the Viterbi path, \mathcal{L} of the original candidate, \mathcal{L} of the single-interferometer runs, and \mathcal{L} of an off-source search.

The off-source search is an additional follow-up procedure. For all 18 outliers, we shift the right ascension by 10' h while keeping all other search parameters fixed. If the candidate is a true astrophysical signal, the resulting log-likelihood should be consistent with Gaussian noise, with probability $1 - \alpha$ of falling below \mathcal{L} threshold. If the off-source search exceeds \mathcal{L}_{th} , there is likely to be an instrumental noise artifact in that band. \mathcal{L} for the single-interferometer runs is included to show whether the candidate is much stronger in one detector than the other. A candidate with a large asymmetry in the reported log-likelihoods from single interferometers can still be indicative of an instrumental noise artifact, even if neither log-likelihood exceeds $\mathcal{L}_{2\text{ifo}}$ in the dual detector run as described in Sec. VA. In particular, we note that \mathcal{L} is mostly higher in the Hanford detector than the Livingston detector. A real signal should not show this behavior, because in O2 Livingston was more sensitive than Hanford [4].

Several of the surviving outliers are close to known instrumental lines, even though outliers of similar frequency are vetoed via the known lines veto in one or more of the other targets. As the \mathcal{F} -statistic accounts for annual and diurnal Doppler modulation, lines that are stationary in the detector frame appear sinusoidal (with a period of a year) after passing through the \mathcal{F} -statistic. Figure 4 shows the recovered Viterbi path for an outlier in SNR G111.7-2.1. Overlaid on the Viterbi path is the predicted Doppler modulation of a stationary noise line as processed by the \mathcal{F} -statistic. The agreement is very good.

Next we briefly discuss all survivors.

1. G18.9-1.1

G18.9-1.1 has two candidates that survive the vetoes. Both show up more strongly in Hanford than Livingston.

The candidate at 462.99 Hz has a log-likelihood of 12342 in H1, versus 8479 in L1. This candidate also

TABLE III. Veto survivors. The second through sixth columns list: the Gaussian threshold log-likelihood, the terminating frequency of the Viterbi path, the dual-interferometer \mathcal{L} , \mathcal{L} from Hanford and Livingston only, and \mathcal{L} of an off-source search. An asterisk indicates that the event is much more significant in one interferometer than the other, and a dagger indicates that the off-source search also produces a candidate above the Gaussian threshold. There are two survivors that are not marked with either a dagger or asterisk, one in G266.2 – 1.2 and one in G347.3 – 0.5. The terminating frequencies of these candidates are similar (445.677 and 446.703), which suggests that these survivors are due to a common noise artifact.

SNR	\mathcal{L}_{th}	Frequency (Hz)	\mathcal{L}	\mathcal{L} H1 only	\mathcal{L} L1 only	\mathcal{L} off-source
G18.9 – 1.1	14830	323.994	16224	12342*	8479	10340.6
		462.986	17321	14363*	8467	17530†
G65.7 + 1.2	5761	68.469	18848	6377	13890*	8498†
		69.997	12818	6412	5925	7275†
		71.996	6440	3972	4337	4695
		323.977	6403	3898	3726	4484
G93.3 + 6.9	15156	463.022	20483	18235*	9585	20683.6†
G189.1 + 30	23227	451.503	43430	28129*	12165	52394†
		491.896	103623	65832*	12212	98998†
		521.749	26651	25177*	13404	25308†
G266.2 – 1.2	47783	19.650	3635140	372352	372352	1085260†
		446.677	49189	28319	22357	48633†
		494.676	79622	47087	47087	100052†
G347.3 – 0.5	45290	446.703	45571	26376	21285	33606
		451.551	89539	59024*	21161	52055†
		501.859	64651000	37762400	3492760	26240600†
		956.293	67043	63642*	21132	34872
		1519.930	48015	43218*	22481	44295

resurfaces as a significant outlier in the off-target search, indicating that it is not of astrophysical origin.

The candidate at 323.99 Hz is very close to an instrumental line, and similar candidates were vetoed for other targets. Therefore we believe this outlier is caused by a noise artifact.

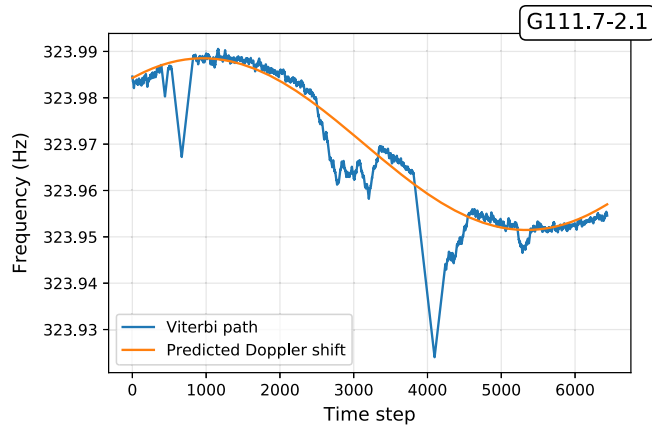


FIG. 4. HMM tracking of a Doppler-shifted instrumental line in the G111.7-2.1 search. The orange curve shows the predicted Doppler shift of a stationary (in the detector frame) noise line processed by the \mathcal{F} -statistic. The blue curve shows the recovered Viterbi path. Note the magnified scale on the vertical axis.

2. G65.7 + 1.2

There are four veto survivors in G65.7 + 1.2. Two of the candidates surpass \mathcal{L}_{th} in the off-source search, and one is much more significant in the Livingston detector than the Hanford detector.

The candidate with a Viterbi path terminating at 71.996 Hz does not appear as an outlier in the off-source search, nor is it much more significant in one detector than in the other. However, comparing the Viterbi path of this candidate to that of the candidate with a terminating frequency of 69.996 Hz, as shown Fig. 5, we see that both paths exhibit similar behavior suggesting a common source e.g., a comb of noise lines [90]. Overlaying the predicted Doppler modulation of a stationary noise line processed by the \mathcal{F} -statistic, we see a strong overlap with the Viterbi path as shown in Fig. 6. Hence we believe this survivor is from an instrumental noise artifact.

The remaining candidate with a terminating frequency of 323.977 Hz lies within ≈ 0.02 Hz of eight other candidates vetoed in other targets. Hence it is likely that the candidate terminating at 323.977 Hz is a noise artifact.

3. G93.3 + 6.9

G93.3 + 6.9 has one survivor, which is much more significant in Hanford than Livingston (18235 versus

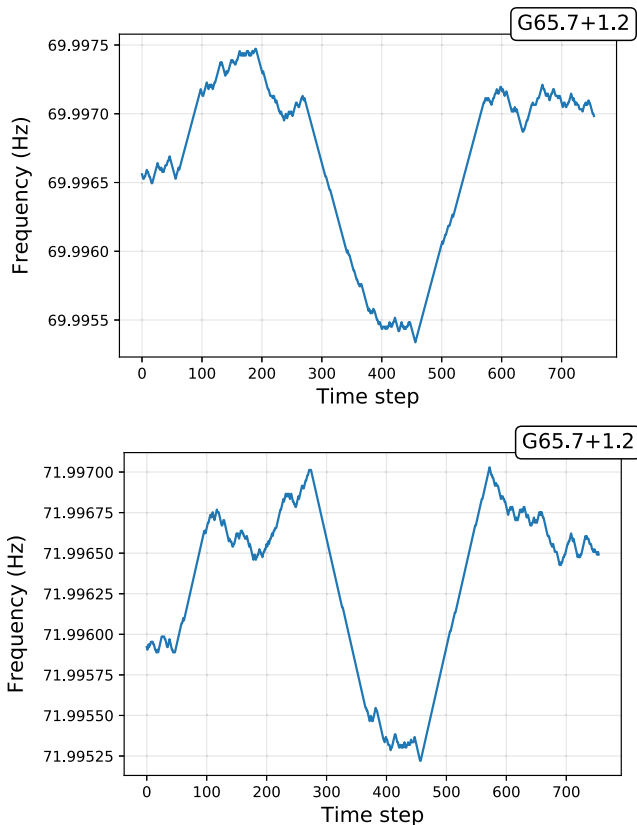


FIG. 5. HMM frequency tracks for two of the outliers in G65.7 + 1.2.

9585) and very significant in the off-source search. Hence, we do not believe it to be a real GW signal.

4. G189.1+3.0

There are three veto survivors in G189.1 + 3.0, with frequencies of approximately 451.50, 491.90, and 521.75 Hz. All three are more significant in Hanford than

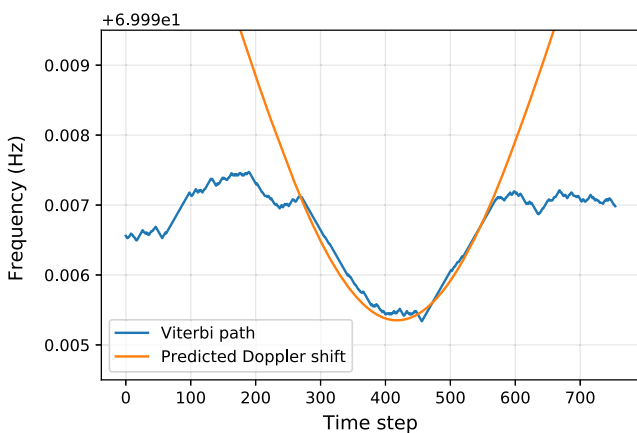


FIG. 6. The recovered Viterbi path for a candidate in G65.7 + 1.2 (blue line) and the predicted Doppler modulation of a stationary noise line (orange line).

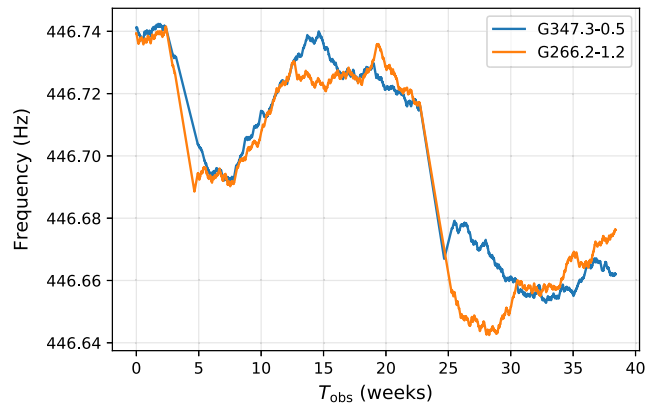


FIG. 7. HMM frequency tracks in the detector frame for two candidates of similar frequency in G266.2 – 1.2 and G347.3 – 0.5. The two Viterbi paths are broadly consistent, indicating that these candidates arise from a common noise artifact. Discrepancies in the paths arise from the different T_{drift} and frequency band resolution used for the two targets.

in Livingston and show up as significant candidates in the off-source search. They are consistent with noise artifacts.

5. G266.2 – 1.2

G266.2 – 1.2 has three survivors. Two of these, at frequencies of 19.65 and 494.68 Hz, are also significant in the off-source search. They are consistent with noise artifacts.

The third candidate is around 446.677 Hz. The single-interferometer and off-source log-likelihoods do not show anything that immediately indicates a noise artifact. However, the target G347.3 – 0.5 independently generates a candidate at a very similar frequency (446.703 Hz). The HMM frequency paths of these candidates in the detector frame are shown in Fig. 7; they are consistent with each other. As there is no reason to believe two different SNRs emit GWs at the same frequency, the signal is unlikely to be astrophysical in origin.

6. G347.3 – 0.5

G347.3 – 0.5 has five survivors. Four of them show up more strongly in Hanford and/or have significant outliers in the off-source search.

As mentioned above, the survivor at 446.703 Hz is very close in frequency to a survivor in the independent SNR G266.2 – 1.2. Both are consistent with noise artifacts.

VI. CONCLUSION

In this work we present a search for continuous GWs from 12 young SNRs using an HMM combined with the maximum-likelihood \mathcal{F} -statistic. This is one of the first searches for these targets in the LIGO O2 dataset. The semicoherent nature of the HMM search confers computational savings, allowing us to use the entire stretch of O2

data. It also ensures that the search is robust to stochastic spin wandering on timescales longer than T_{drift} , with $1\text{h} \leq T_{\text{drift}} \leq 8.5\text{h}$.

For each target, we select the search band and coherent analysis time T_{drift} to maximize the GW discovery potential. After performing data quality vetoes, we find surviving candidates in six SNR targets. Off-source searches and manual follow-up of these survivors indicates that all of them are due to instrumental noise artifacts and not GWs.

Some previous HMM searches have placed upper limits on the strain of the GWs emitted by the target of the search [53,54]. These limits follow from Monte Carlo simulations to determine the minimum detectable h_0 (at 95% confidence). Roughly 1000 signals of varying h_0 are injected into different noise realizations, and this process is repeated across a number of subbands. As this work involves 12 targets, each covering a wide frequency range with months of data, such an upper limit study becomes computationally expensive. Additionally, the phase model in the HMM search is a random walk. Therefore any upper limits are not directly comparable with previous searches where the signal model is based on a Taylor expansion of the phase; in general, upper limits are conditional on the signal model in any search. For these reasons, we do not produce upper limits in this work.

Just before submitting this manuscript, we became aware of a search for young SNRs by Lindblom and Owen [15]. The two searches are similar in some ways, but there are four important differences:

- (1) They are directed at overlapping but distinct sets of targets. Specifically, targets searched in [15] but not in this work are $G15.9 + 0.2$, $G39.2 - 0.3$, and $G353.6 - 0.7$. Not included in [15] are searches for the targets $G111.7 - 2.1$, $G266.2 - 1.2$, and $G347.3 - 0.5$ (though these targets were searched in [13]).
- (2) They search different bands. The search presented in [15] examines the band between 15 and 150 Hz for all targets in order to accommodate a fixed computational cost. In this work the frequency band varies by target (see Table I). The narrowest frequency band searched is 35–122 Hz for $G1.9 + 0.3$, and the widest band is 23–1747 Hz for $G347.3 - 0.5$. With two exceptions ($G1.9 + 0.3$ and $G354.4 + 0.0$), the bands in this search are wider.
- (3) They analyze different volumes of data. The search presented in [15] uses a different observation time for each target. The range of these observation times is 12–55.9 days. The search presented in this paper uses all available O2 data, as outlined in Sec. IV C.
- (4) The HMM search is semicoherent and robust against spin wandering, whereas the work presented in [15] uses a coherent matched filter.

For all these reasons, the two analyses are complementary without being easily comparable. A comparative study of the sensitivities, even within their common band, is a tricky exercise to be attempted in future work.

LIGO is currently in its third observing run, O3, and is expected to improve its sensitivity relative to O2. More data at higher sensitivity increases our chances of making a detection of periodic GWs. The HMM search can also be improved for rapidly spinning down SNR targets by tracking f_0 as well as \dot{f}_0 [43].

ACKNOWLEDGMENTS

Parts of this research were conducted by the Australian Research Council Centre of Excellence for Gravitational Wave Discovery (OzGrav), through Project No. CE170100004. This research has made use of data, software and/or web tools obtained from the Gravitational Wave Open Science Center, a service of LIGO Laboratory, the LIGO Scientific Collaboration and the Virgo Collaboration. LIGO is funded by the U.S. National Science Foundation. Virgo is funded by the French Centre National de Recherche Scientifique (CNRS), the Italian Istituto Nazionale della Fisica Nucleare (INFN) and the Dutch Nikhef, with contributions by Polish and Hungarian institutes. We thank the Continuous Wave Working Group of the LIGO Scientific Collaboration and Virgo Collaboration for their helpful discussion, and in particular Karl Wette and David Keitel for their helpful comments. We also thank Hannah Middleton, Patrick Clearwater, Pat Meyers, and Lilli Sun for informative discussions.

APPENDIX: HARDWARE INJECTIONS

To validate data analysis pipelines and calibration, simulated signals can be added to the LIGO detectors. These are commonly called hardware injections. In O2, injections were added to simulate GW signals from isolated rotating neutron stars [30,91]. One such hardware injection is picked up by our search for the SNR target $G330.2 + 1.0$. This candidate is from injected pulsar 6, as described in Ref. [7]. Loud hardware injections have previously been detected at incorrect sky locations [12]. As in this work, this

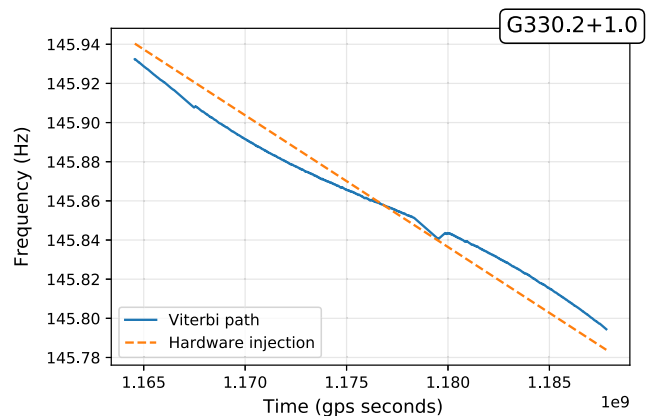


FIG. 8. Viterbi path corresponding to a hardware injection.

TABLE IV. Details of hardware injection candidate. The table lists the threshold log-likelihood for each target with remaining outliers, the terminating frequency of the candidate path, \mathcal{L} of the outlier, \mathcal{L} of the H1 and L1 only runs, and \mathcal{L} of an off-source search.

SNR	L_{th}	Frequency (Hz)	\mathcal{L}	\mathcal{L} H1 only	\mathcal{L} L1 only	\mathcal{L} off-source
G330.2 + 1.0	23346	145.794	23452	17350	16344	12112

particular injection was found in multiple targets in Ref. [15].

The Viterbi path for this candidate, along with the frequency evolution of the hardware injection, is shown

in Fig. 8. \mathcal{L} for the candidate, the single-interferometer runs, and the off-source run are shown in Table IV. We include the results to illustrate how a true GW signal would behave.

-
- [1] K. Riles, Gravitational waves: Sources, detectors and searches, *Prog. Part. Nucl. Phys.* **68**, 1 (2013).
- [2] G. M. Harry *et al.* (LIGO Scientific Collaboration), Advanced LIGO: The next generation of gravitational wave detectors, *Classical Quantum Gravity* **27**, 084006 (2010).
- [3] J. Aasi, B. P. Abbott, R. Abbott, T. Abbott, M. R. Abernathy, K. Ackley, C. Adams, T. Adams, P. Addesso *et al.* (LIGO Scientific Collaboration), Advanced LIGO, *Classical Quantum Gravity* **32**, 074001 (2015).
- [4] B. P. Abbott *et al.*, GWTC-1: A Gravitational-Wave Transient Catalog of Compact Binary Mergers Observed by LIGO and Virgo During the First and Second Observing Runs, *Phys. Rev. X* **9**, 031040 (2019).
- [5] B. P. Abbott *et al.* (LIGO Scientific and Virgo Collaborations), First low-frequency einstein@home all-sky search for continuous gravitational waves in Advanced LIGO data, *Phys. Rev. D* **96**, 122004 (2017).
- [6] V. Dergachev and M. A. Papa, Results from an extended falcon all-sky survey for continuous gravitational waves, *Phys. Rev. D* **101**, 022001 (2020).
- [7] B. P. Abbott *et al.* (LIGO Scientific and Virgo Collaborations), All-sky search for continuous gravitational waves from isolated neutron stars using Advanced LIGO o2 data, *Phys. Rev. D* **100**, 024004 (2019).
- [8] B. P. Abbott *et al.* (LIGO Scientific and Virgo Collaborations), First narrow-band search for continuous gravitational waves from known pulsars in advanced detector data, *Phys. Rev. D* **96**, 122006 (2017).
- [9] B. P. Abbott *et al.* (LIGO Scientific and Virgo Collaborations), Narrow-band search for gravitational waves from known pulsars using the second LIGO observing run, *Phys. Rev. D* **99**, 122002 (2019).
- [10] J. Aasi *et al.* (LIGO Scientific and Virgo Collaborations), Directed search for continuous gravitational waves from the galactic center, *Phys. Rev. D* **88**, 102002 (2013).
- [11] O. J. Piccinni, P. Astone, S. D’Antonio, S. Frasca, G. Intini, I. La Rosa, P. Leaci, S. Mastrogiovanni, A. Miller, and C. Palomba, A directed search for continuous gravitational-wave signals from the galactic center in Advanced LIGO second observing run, *Phys. Rev. D* **101**, 082004 (2020).
- [12] B. P. Abbott, R. Abbott, T. D. Abbott, S. Abraham, F. Acernese, K. Ackley, C. Adams, R. X. Adhikari, V. B. Adya, C. Affeldt *et al.*, Searches for continuous gravitational waves from 15 supernova remnants and fomalhaut b with Advanced LIGO, *Astrophys. J.* **875**, 122 (2019).
- [13] J. Ming, M. A. Papa, A. Singh, H.-B. Eggenstein, S. J. Zhu, V. Dergachev, Y. Hu, R. Prix, B. Machenschalk, C. Beer, O. Behnke, and B. Allen, Results from an einstein@home search for continuous gravitational waves from cassiopeia a, vela jr., and g347.3, *Phys. Rev. D* **100**, 024063 (2019).
- [14] S. J. Zhu, M. A. Papa, H.-B. Eggenstein, R. Prix, K. Wette, B. Allen, O. Bock, D. Keitel, B. Krishnan, B. Machenschalk, M. Shaltev, and X. Siemens, Einstein@Home search for continuous gravitational waves from Cassiopeia A, *Phys. Rev. D* **94**, 082008 (2016).
- [15] L. Lindblom and B. J. Owen, Directed searches for continuous gravitational waves from twelve supernova remnants in data from Advanced LIGO’s second observing run, *Phys. Rev. D* **101**, 083023 (2020).
- [16] B. Knispel and B. Allen, Blandford’s argument: The strongest continuous gravitational wave signal, *Phys. Rev. D* **78**, 044031 (2008).
- [17] A. I. Chugunov and C. J. Horowitz, Breaking stress of neutron star crust, *Mon. Not. R. Astron. Soc. Lett.* **407**, L54 (2010).
- [18] K. Wette, M. Vigelius, and A. Melatos, Sinking of a magnetically confined mountain on an accreting neutron star, *Mon. Not. R. Astron. Soc.* **402**, 1099?1110 (2010).
- [19] G. Ushomirsky, C. Cutler, and L. Bildsten, Deformations of accreting neutron star crusts and gravitational wave emission, *Mon. Not. R. Astron. Soc.* **319**, 902 (2000).
- [20] N. K. Johnson-McDaniel and B. J. Owen, Maximum elastic deformations of relativistic stars, *Phys. Rev. D* **88**, 044004 (2013).
- [21] C. Cutler, Gravitational waves from neutron stars with large toroidal B fields, *Phys. Rev. D* **66**, 084025 (2002).
- [22] A. Mastrano, A. Melatos, A. Reisenegger, and T. Akgün, Gravitational wave emission from a magnetically deformed non-barotropic neutron star, *Mon. Not. R. Astron. Soc.* **417**, 2288 (2011).

- [23] P. D. Lasky and A. Melatos, Tilted torus magnetic fields in neutron stars and their gravitational wave signatures, *Phys. Rev. D* **88**, 103005 (2013).
- [24] D. I. Jones, Gravitational wave emission from rotating superfluid neutron stars, *Mon. Not. R. Astron. Soc.* **402**, 2503 (2010).
- [25] A. Melatos, J. A. Douglass, and T. P. Simula, Persistent gravitational radiation from glitching pulsars, *Astrophys. J. Lett.* **807**, 132 (2015).
- [26] S. Caride, R. Inta, B. J. Owen, and B. Rajbhandari, How to search for gravitational waves from r -modes of known pulsars, *Phys. Rev. D* **100**, 064013 (2019).
- [27] J. Aasi, B. P. Abbott, R. Abbott, T. Abbott, M. R. Abernathy, F. Acernese, K. Ackley, C. Adams, T. Adams, P. Addesso *et al.*, Searches for continuous gravitational waves from nine young supernova remnants, *Astrophys. J.* **813**, 39 (2015).
- [28] J. M. Cordes, Limits to PTA sensitivity: spin stability and arrival time precision of millisecond pulsars, *Classical Quantum Gravity* **30**, 224002 (2013).
- [29] S. Suvorova, L. Sun, A. Melatos, W. Moran, and R. J. Evans, Hidden Markov model tracking of continuous gravitational waves from a neutron star with wandering spin, *Phys. Rev. D* **93**, 123009 (2016).
- [30] M. Vallisneri, J. Kanner, R. Williams, A. Weinstein, and B. Stephens, The LIGO open science center, *J. Phys. Conf. Ser.* **610**, 012021 (2015).
- [31] R. Abbott *et al.* (LIGO Scientific and Virgo Collaborations), Open data from the first and second observing runs of Advanced LIGO and Advanced Virgo, [arXiv:1912.11716](https://arxiv.org/abs/1912.11716).
- [32] J. Abadie, B. P. Abbott, R. Abbott, M. Abernathy, C. Adams, R. Adhikari, P. Ajith, B. Allen, G. Allen, E. A. Ceron *et al.*, First search for gravitational waves from the youngest known neutron star, *Astrophys. J.* **722**, 1504 (2010).
- [33] L. Sun, A. Melatos, P. D. Lasky, C. T. Y. Chung, and N. S. Darman, Cross-correlation search for continuous gravitational waves from a compact object in SNR 1987A in LIGO Science run 5, *Phys. Rev. D* **94**, 082004 (2016).
- [34] P. Jaranowski, A. Królak, and B. Schutz, Data analysis of gravitational-wave signals from spinning neutron stars: The signal and its detection, *Phys. Rev. D* **58**, 063001 (1998).
- [35] LIGO Scientific Collaboration, LIGO Algorithm Library—LALSuite, free software (GPL) (2018).
- [36] R. Prix, The F-statistic and its implementation in ComputeFStatistic_v2, LIGO Technical Document T0900149 (2018).
- [37] G. Hobbs, A. G. Lyne, and M. Kramer, An analysis of the timing irregularities for 366 pulsars, *Mon. Not. R. Astron. Soc.* **402**, 1027 (2010).
- [38] R. M. Shannon and J. M. Cordes, Assessing the role of spin noise in the precision timing of millisecond pulsars, *Astrophys. J.* **725**, 1607 (2010).
- [39] G. Ashton, D. I. Jones, and R. Prix, Effect of timing noise on targeted and narrow-band coherent searches for continuous gravitational waves from pulsars, *Phys. Rev. D* **91**, 062009 (2015).
- [40] S. Dhurandhar, B. Krishnan, H. Mukhopadhyay, and J. T. Whelan, Cross-correlation search for periodic gravitational waves, *Phys. Rev. D* **77**, 082001 (2008).
- [41] B. Krishnan, A. M. Sintes, M. Alessandra Papa, B. F. Schutz, S. Frasca, and C. Palomba, Hough transform search for continuous gravitational waves, *Phys. Rev. D* **70**, 082001 (2004).
- [42] E. Goetz and K. Riles, An all-sky search algorithm for continuous gravitational waves from spinning neutron stars in binary systems, *Classical Quantum Gravity* **28**, 215006 (2011).
- [43] L. Sun, A. Melatos, S. Suvorova, W. Moran, and R. J. Evans, Hidden markov model tracking of continuous gravitational waves from young supernova remnants, *Phys. Rev. D* **97**, 043013 (2018).
- [44] J. M. Cordes and D. J. Helfand, Pulsar timing. III. Timing noise of 50 pulsars, *Astrophys. J.* **239**, 640 (1980).
- [45] G. Hobbs, A. G. Lyne, and M. Kramer, An analysis of the timing irregularities for 366 pulsars, *Mon. Not. R. Astron. Soc.* **402**, 1027 (2010).
- [46] A. Melatos, Spin-down of an oblique rotator with a current-starved outer magnetosphere, *Mon. Not. R. Astron. Soc.* **288**, 1049 (1997).
- [47] L. Bildsten, D. Chakrabarty, J. Chiu, M. H. Finger, D. T. Koh, R. W. Nelson, T. A. Prince, B. C. Rubin, D. M. Scott, M. Stollberg, B. A. Vaughan, C. A. Wilson, and R. B. Wilson, Observations of accreting pulsars, *Astrophys. J. Suppl. Ser.* **113**, 367 (1997).
- [48] A. Viterbi, Error bounds for convolutional codes and an asymptotically optimum decoding algorithm, *IEEE Trans. Inf. Theory* **13**, 260 (1967).
- [49] K. Wette *et al.*, Searching for gravitational waves from Cassiopeia a with LIGO, *Classical Quantum Gravity* **25**, 235011 (2008).
- [50] B. J. Owen, Search templates for gravitational waves from inspiraling binaries: Choice of template spacing, *Phys. Rev. D* **53**, 6749 (1996).
- [51] P. R. Brady, T. Creighton, C. Cutler, and B. F. Schutz, Searching for periodic sources with LIGO, *Phys. Rev. D* **57**, 2101 (1998).
- [52] R. Prix, Search for continuous gravitational waves: Metric of the multidetector F-statistic, *Phys. Rev. D* **75**, 023004 (2007).
- [53] B. P. Abbott, R. Abbott, T. D. Abbott, F. Acernese, K. Ackley, C. Adams, T. Adams, P. Addesso, R. X. Adhikari, V. B. Adya *et al.*, Search for gravitational waves from Scorpius X-1 in the first Advanced LIGO observing run with a hidden Markov model, *Phys. Rev. D* **95**, 122003 (2017).
- [54] B. P. Abbott *et al.* (LIGO Scientific and Virgo Collaborations), Search for gravitational waves from Scorpius X-1 in the second Advanced LIGO observing run with an improved hidden Markov model, *Phys. Rev. D* **100**, 122002 (2019).
- [55] H. Middleton, P. Clearwater, A. Melatos, and L. Dunn, Search for gravitational waves from five low mass X-ray binaries in the second Advanced LIGO observing run with an improved hidden Markov model, *Phys. Rev. D* **102**, 023006 (2020).
- [56] B. P. Abbott, R. Abbott, T. D. Abbott, F. Acernese, K. Ackley, C. Adams, T. Adams, P. Addesso, R. X. Adhikari, V. B. Adya *et al.*, Search for gravitational waves from a long-lived remnant of the binary neutron star merger gw170817, *Astrophys. J.* **875**, 160 (2019b).

- [57] Z. Arzoumanian, A. S. Fruchter, and J. H. Taylor, Orbital variability in the eclipsing pulsar binary PSR B1957 + 20, *Astrophys. J. Lett.* **426**, L85 (1994).
- [58] R. F. Archibald, E. V. Gotthelf, R. D. Ferdman, V. M. Kaspi, S. Guillot, F. A. Harrison, E. F. Keane, M. J. Pivovarov, D. Stern, S. P. Tendulkar, and J. A. Tomsick, A high braking index for a pulsar, *Astrophys. J. Lett.* **819**, L16 (2016).
- [59] D. A. Green, A revised catalogue of 294 Galactic supernova remnants, *J. Astrophys. Astron.* **40**, 36 (2019).
- [60] LIGO Scientific Collaboration, SFT data format version 2 specification (2004).
- [61] S. P. Reynolds, K. J. Borkowski, D. A. Green, U. Hwang, I. Harrus, and R. Petre, The youngest galactic supernova remnant: G1.9 + 0.3, *Astrophys. J.* **680**, L41 (2008).
- [62] D. A. Green and S. F. Gull, Two new young galactic supernova remnants, *Nature (London)* **312**, 527 (1984).
- [63] R. Türlmann, P. P. Plucinsky, T. J. Gaetz, P. Slane, J. P. Hughes, I. Harrus, and T. G. Pannuti, Searching for the pulsar in g18.95-1.1: Discovery of an x-ray point source and associated synchrotron nebula withchandra, *Astrophys. J.* **720**, 848 (2010).
- [64] I. M. Harrus, P. O. Slane, J. P. Hughes, and P. P. Plucinsky, An x-ray study of the supernova remnant G18.95-1.1, *Astrophys. J.* **603**, 152 (2004).
- [65] R. Kothes, T. L. Landecker, and M. Wolleben, H I absorption of polarized emission: A new technique for determining kinematic distances to galactic supernova remnants, *Astrophys. J.* **607**, 855 (2004).
- [66] R. Kothes, T. L. Landecker, W. Reich, S. Safi-Harb, and Z. Arzoumanian, DA 495: An aging pulsar wind nebula, *Astrophys. J.* **687**, 516 (2008).
- [67] B. Jiang, Y. Chen, and Q. D. Wang, The Chandra view of DA 530: A subenergetic supernova remnant with a pulsar wind nebula?, *Astrophys. J.* **670**, 1142 (2007).
- [68] T. Foster and D. Routledge, A new distance technique for galactic plane objects, *Astrophys. J.* **598**, 1005 (2003).
- [69] H. Tananbaum, Cassiopeia A, IAU Circulars **7246**, 1 (1999).
- [70] J. E. Reed, J. J. Hester, A. C. Fabian, and P. F. Winkler, The three-dimensional structure of the Cassiopeia a Supernova remnant. I. The spherical shell, *Astrophys. J.* **440**, 706 (1995).
- [71] R. A. Fesen, M. C. Hammell, J. Morse, R. A. Chevalier, K. J. Borkowski, M. A. Dopita, C. L. Gerardy, S. S. Lawrence, J. C. Raymond, and S. van den Bergh, The expansion asymmetry and age of the Cassiopeia a supernova remnant, *Astrophys. J.* **645**, 283 (2006).
- [72] D. A. Swartz, G. G. Pavlov, T. Clarke, G. Castelletti, V. E. Zavlin, N. Bucciantini, M. Karovska, A. J. van der Horst, M. Yukita, and M. C. Weisskopf, High spatial resolution x-ray spectroscopy of the IC 443 pulsar wind nebula and environs, *Astrophys. J.* **808**, 84 (2015).
- [73] C. M. Olbert, C. R. Clearfield, N. E. Williams, J. W. Keohane, and D. A. Frail, A bow shock nebula around a compact x-ray source in the supernova remnant IC 443, *Astrophys. J. Lett.* **554**, L205 (2001).
- [74] G. G. Pavlov, D. Sanwal, B. Kızıltan, and G. P. Garmire, The compact central object in the RX J0852.0-4622 supernova remnant, *Astrophys. J. Lett.* **559**, L131 (2001).
- [75] G. E. Allen, K. Chow, T. DeLaney, M. D. Filipović, J. C. Houck, T. G. Pannuti, and M. D. Stage, On the expansion rate, age, and distance of the supernova remnant G266.2-1.2 (Vela Jr.), *Astrophys. J.* **798**, 82 (2015).
- [76] P. Slane, J. P. Hughes, T. Temim, R. Rousseau, D. Castro, D. Foight, B. M. Gaensler, S. Funk, M. Lemoine-Goumard, J. D. Gelfand, D. A. Moffett, R. G. Dodson, and J. P. Bernstein, A broadband study of the emission from the composite supernova remnant MSH 11-62, *Astrophys. J.* **749**, 131 (2012).
- [77] D. Moffett, B. Gaensler, and A. Green, G291.0-0.1: Powered by a pulsar? in *Young Supernova Remnants*, edited by Stephen S. Holt and U. Hwang, American Institute of Physics Conference Series Vol. 565 (AIP, Melville, 2001), pp. 333–336.
- [78] S. Park, K. Mori, O. Kargaltsev, P. O. Slane, J. P. Hughes, D. N. Burrows, G. P. Garmire, and G. G. Pavlov, Discovery of a candidate central compact object in the galactic non-thermal SNR G330.2 + 1.0, *Astrophys. J. Lett.* **653**, L37 (2006).
- [79] N. M. McClure-Griffiths, A. J. Green, John M. Dickey, B. M. Gaensler, R. F. Haynes, and M. H. Wieringa, The southern galactic Plane survey: The test region, *Astrophys. J.* **551**, 394 (2001).
- [80] R. P. Mignani, S. Zaggia, A. de Luca, R. Perna, N. Bassan, and P. A. Caraveo, Optical and infrared observations of the X-ray source 1WGA J1713.4-3949 in the G347.3-0.5 SNR, *J. Astrophys. Astron.* **484**, 457 (2008).
- [81] G. Cassam-Chenaï, A. Decourchelle, J. Ballet, J. L. Sauvageot, G. Dubner, and E. Giacani, XMM-Newton observations of the supernova remnant RX J1713.7-3946 and its central source, *J. Astrophys. Astron.* **427**, 199 (2004).
- [82] Z. R. Wang, Q. Y. Qu, and Y. Chen, Is RX J1713.7-3946 the remnant of the AD393 guest star?, *J. Astrophys. Astron.* **318**, L59 (1997).
- [83] B. M. Gaensler, A. Tanna, P. O. Slane, C. L. Brogan, J. D. Gelfand, N. M. McClure-Griffiths, F. Camilo, C. Y. Ng, and J. M. Miller, The (re-)discovery of G350.1-0.3: A young, luminous supernova remnant and its neutron star, *Astrophys. J. Lett.* **680**, L37 (2008).
- [84] I. Lovchinsky, P. Slane, B. M. Gaensler, J. P. Hughes, C. Y. Ng, J. S. Lazendic, J. D. Gelfand, and C. L. Brogan, A Chandra observation of supernova remnant G350.1-0.3 and its central compact object, *Astrophys. J.* **731**, 70 (2011).
- [85] S. Roy and S. Pal, Discovery of the small-diameter, young supernova remnant G354.4 + 0.0, *Astrophys. J.* **774**, 150 (2013).
- [86] W. W. Swart, C. E. Gearing, and T. Var, A dynamic programming—Integer programming algorithm for allocating touristic investments, *Tourist Rev.* **27**, 52 (1972).
- [87] LIGO Scientific and Virgo Collaborations, Open data from advanced LIGO's second observing run, <https://doi.org/10.7935/CA75-FM95> (2019).
- [88] B. P. Abbott, R. Abbott, T. D. Abbott, M. R. Abernathy, F. Acernese, K. Ackley, M. Adamo, C. Adams, T. Adams, P. Addesso *et al.*, Characterization of transient noise in Advanced LIGO relevant to gravitational wave signal gw150914, *Classical Quantum Gravity* **33**, 134001 (2016).
- [89] B. P. Abbott *et al.*, Effects of data quality vetoes on a search for compact binary coalescences in Advanced LIGO's first observing run, *Classical Quantum Gravity* **35**, 065010 (2018).

- [90] P. B. Covas, A. Effler, E. Goetz, P. M. Meyers, A. Neunzert, M. Oliver, B. L. Pearlstone, V. J. Roma, R. M. S. Schofield, V. B. Adya *et al.*, Identification and mitigation of narrow spectral artifacts that degrade searches for persistent gravitational waves in the first two observing runs of Advanced LIGO, *Phys. Rev. D* **97**, 082002 (2018).
- [91] C. Biwer, D. Barker, J. C. Batch, J. Betzwieser, R. P. Fisher, E. Goetz, S. Kandhasamy, S. Karki, J. S. Kissel, A. P. Lundgren *et al.*, Validating gravitational-wave detections: The Advanced LIGO hardware injection system, *Phys. Rev. D* **95**, 062002 (2017).